

Binary Mixtures of Intelligent Active Brownian Particles with Visual Perception*

Rajendra Singh Negi,^{1, 2, †} Roland G. Winkler,^{1, ‡} and Gerhard Gompper^{1, §}

¹*Theoretical Physics of Living Matter, Institute for Advanced Simulation,
Forschungszentrum Jülich, 52425 Jülich, Germany*

²*Department of Physics, Syracuse University, Syracuse, New York 13244, USA*

(Dated: June 12, 2025)

The collective properties of a binary mixture of *A*- and *B*-type self-steering particles endowed with visual perception are studied by computer simulations. Active Brownian particles are employed with an additional steering mechanism, which enables them to adjust their propulsion direction relative to the instantaneous positions of neighboring particles, depending on the species, either steering toward or away from them. Steering can be nonreciprocal between the *A*- and *B*-type particles. The underlying dynamical and structural properties of the system are governed by the strength and polarity of the maneuverabilities associated with the vision-induced steering. The model predicts the emergence of a large variety of nonequilibrium behaviors, which we systematically characterize for all nine principal sign combinations of *AA*, *BB*, *AB* and *BA* maneuverabilities. In particular, we observe the formation of multimers, encapsulated aggregates, honeycomb lattices, and predator-prey pursuit. Notably, for a predator-prey system, the maneuverability and vision angle employed by a predator significantly impacts the spatial distribution of the surrounding prey particles. For systems with electric-charge-like interactions and non-stoichiometric composition, we obtain at intermediate activity levels an enhanced diffusion compared to non-steering active Brownian particles.

I. INTRODUCTION

Active-matter systems, ranging from microscopic biological systems such as bacteria [1–3] to macroscopic biological systems as flocks of birds [4–6], are intrinsically out of equilibrium and show a vast variety of fascinating emergent behaviors [7–10]. Such features are not restricted to biological systems, but have been partially reproduced in artificial and hybrid systems, specifically in those comprised of Janus colloids [11–13]. This makes active matter an important research field with significant biomedical potential, e.g., targeted drug delivery using engineered bacteria for tumor therapy [14] and biomedical untethered mobile milli/microrobots capable of accessing previously unreachable single cell sites for *in situ* and *in vivo* applications [15]. It also offers promising solutions for environmental improvements, such as water treatment [16, 17]. Arising patterns and structures not only depend on the physical interactions between the various agents of an ensemble, but are often governed by nonreciprocal information input, e.g., directional visual perception in case of animals, processing of this information, and active self-steering response.

Multi-component mixtures of self-steering active agents with nonreciprocal interactions can show an even more intriguing behavior. It is important to note that the nonreciprocal nature of interactions in multi-component systems is on a different level compared to single-component systems, because the reaction of particles of one species to a particle of another species can be

different from the inverse reaction [18–21].

Binary mixtures of active agents are prevalent in biological systems. For example, mixed swarms of bacteria *Bacillus subtilis* and *Pseudomonas aeruginosa* exhibit both cooperation and segregation across scales [22]. Mixtures of two strains of *B. subtilis* with distinct cell aspect-ratios show aggregate formation, in which longer cells serve as nucleation sites, attracting shorter and highly mobile cells [23]. Mixing motile and nonmotile *Escherichia coli* bacteria results in active density changes, where the circular movement of motile cells near surfaces creates flowing patterns that carry nonmotile cells along, while sedimentation disrupts vertical symmetry, crucial for their gathering [24]. Interactions between marine *Pseudoalteromonas* sp. and Gram-positive bacteria show predator-prey behavior, where the predator uses enzymes to kill Gram-positive cells while coexisting peacefully with Gram-negative bacteria, revealing how microbes can both compete and cooperate within mixed communities [25]. Recent experimental evidence indeed suggests that swimming and chemotactic sensing play an important role in shaping interbacterial interactions [26]. Furthermore, the relevance of sensing and self-steering is evident in macroscale binary biological systems. For instance, the flight of bee swarms to new nests consists of a binary mixture of stayer (leader) bees and follower (uninformed) bees, where bees use directed vision for attraction and repulsion among themselves [27, 28]. Also, there are many examples of large animals hunting others, like wolves chasing deer or sharks hunting fish swarms. In synthetic systems, chemotactic signaling in a mixture of microscale oil droplets of different chemistry embedded in micellar surfactant solutions have been shown to create predator-prey-like nonreciprocal chasing interactions [21, 29, 30].

Theoretical and simulation studies of model systems

* Electronic supplement available

† ranegi@syr.edu

‡ rg_winkler@gmx.de

§ g.gompper@fz-juelich.de

provide essential insight into the complex emergent behavior of active systems in general and binary mixtures of self-steering particles in particular. They facilitate the characterization of the emergent structures and dynamics and their dependence on the agent properties. Ultimately, they can provide a guide for the rational design of synthetic active agents with desired properties.

“Dumb” active Brownian particles (ABPs) – with conservative interactions only, like hard-core repulsion – display aggregation in the form of motility-induced phase separation (MIPS) [31–34] and nonequilibrium clustering in presence of hydrodynamic interactions [35, 36]. Already binary mixtures of such active and passive Brownian particles show phase separation with domains enriched by passive or active particles, and propagating interfaces between them [37–40]. Experimental studies demonstrate that passive silica colloids rapidly self-assemble into tunable 2D structures via diffusiophoretic interactions with UV-activated Janus particles, with the clustering dynamics controlled by light intensity and particle size ratios [41]. Along the same line, simulations by varying the active particle density reveal a non-monotonic clustering trend, where high activity leads to an effective screening of phoretic interactions, slowing down aggregation [42].

In systems with alignment of the propulsion direction with neighboring particles, as in the Vicsek model [6], collective motion in single-component systems has been predicted in form of travelling bands [6]. The incorporation of anisotropic sensory perception in that model significantly impacts the system’s collective behavior [43]. In single-component self-steering systems with pursuit-type steering, an even more complex behavior can emerge, such as milling [44, 45], and the formation of worm-like structures and worm-aggregate coexistence [44, 46–49]. Variants of the Vicsek model with two distinct species, for example systems of slow- and fast-moving self-propelled particles, where particles align within their own species and antialign with the other, yield micro-phase separation and parallel/antiparallel bands [50], while mixtures of active and passive particles with local alignment in confinement display segregation into an active core and a passive shell [51].

The emergent behavior becomes even more intriguing for active mixtures with nonreciprocal interactions between particle types. A prominent example is a mixture of chemically interacting particles, which produce or consume a chemical to which they are attracted or repelled corresponding to positive or negative chemotaxis. Such systems display a wealth of active clustering and phase-separation phenomena, such as association of particles into small molecules, aggregation into a static dense phase that coexists with a dilute phase, and the formation of non-stoichiometric self-propelled macroscopic clusters with a comet-like tail [52]. Self-propulsion heterogeneity and nonreciprocity of binary interactions can drive the partial segregation of mixtures of active colloids [53].

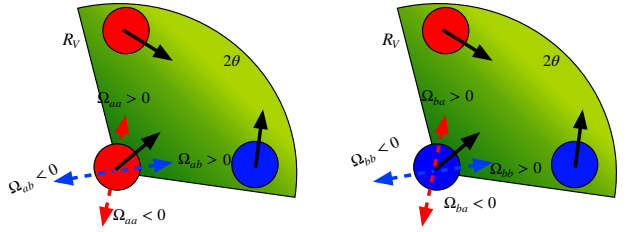


FIG. 1. Schematic representation of the vision cone of a particle of the two types, A (red) and B (blue), and their corresponding maneuverabilities. The dashed arrows indicate the nature of steering toward and away from detected particles within the vision cone.

Here, we explore the collective behavior and structure formation of binary mixtures of active particles with visual perception and nonreciprocal self-steering. An agent is modeled as an “intelligent” active Brownian particle (iABP), with implicit self-steering abilities. An iABP can move toward or away from its own or the other species, with limited maneuverability Ω , by sensing the positions of neighboring particles in its vision cone, as illustrated in Fig. 1. Despite the considered minimal model, our approach contains a significant number of parameters, such as the activities of the two particle species, their vision angles and steering ability, the particle densities etc. This results in a rich phase behavior and interesting dynamics, which we are unable to characterize completely here. Instead, we focus on various parameter combinations, which illustrate intriguing emergent behaviors.

II. MODELLING BINARY MIXTURES OF INTELLIGENT ABPS

A. Equations of motion

In our minimalistic approach, the two types *A* and *B* of agents are described as self-steering active Brownian particles with visual perception. A mixture is composed of the total number $N = N_A + N_B$ of particles. The particle dynamics is governed by the equations of motion [44, 48, 54]

$$m\ddot{\mathbf{r}}_i = -\gamma_T \dot{\mathbf{r}}_i + \gamma_T v_0 \mathbf{e}_i + \mathbf{F}_i + \boldsymbol{\Gamma}_i(t), \quad (1)$$

where $\mathbf{F}_i^a(t) = \gamma_T v_0 \mathbf{e}_i(t)$ is the propulsion force resulting in a speed v_0 along the direction $\mathbf{e}_i(t)$, which can change in response to the sensed environment. Moreover, m is the mass of an iABP, γ_T the translational friction coefficient, and \mathbf{F}_i the excluded-volume interactions between the iABPs. The latter are taken into account by the truncated and shifted Lennard-Jones potential

$$U_{LJ} = \begin{cases} 4\epsilon \left[\left(\frac{\sigma}{r} \right)^{12} - \left(\frac{\sigma}{r} \right)^6 + 1 \right] + \epsilon, & r \leq 2^{1/6}\sigma \\ 0, & r > \sigma. \end{cases} \quad (2)$$

Here, σ is the particle diameter, ϵ the repulsion strength, and r the distance between two iABPs. Thermal fluctuations are considered as Gaussian and Markovian stochastic process $\boldsymbol{\Gamma}_i$ of zero mean and the second moments $\langle \boldsymbol{\Gamma}_i(t) \cdot \boldsymbol{\Gamma}_j(t') \rangle = 2d\gamma_T k_B T \delta(t-t') \delta_{ij}$ in d dimensions, with T the temperature and k_B the Boltzmann constant.

An iABP is capability to respond to information regarding the position of the neighboring particles within a vision cone by adjusting its propulsion direction. Figure 1 illustrates the vision cones for a A - (red) particle and a B - (blue) particle, respectively, along with their respective capability (maneuverability) to respond to the instantaneous positions of their neighbors.

The evolution of the propulsion direction $\boldsymbol{e}_i^\alpha(t)$ of particle i of type α ($\alpha, \beta \in \{A, B\}$, $\alpha \neq \beta$) is governed by [48, 55]

$$\dot{\boldsymbol{e}}_i^\alpha(t) = \sum_{\gamma \in \{\alpha, \beta\}} \boldsymbol{M}_i^{\alpha\gamma} + \boldsymbol{\Lambda}_i(t) \times \boldsymbol{e}_i^\alpha(t). \quad (3)$$

The last term describes the (thermal) rotational diffusion independent of the particle type. It is modeled as Gaussian and Markovian stochastic processes of zero mean, variance $\langle \boldsymbol{\Lambda}_i(t) \cdot \boldsymbol{\Lambda}_j(t') \rangle = 2(d-1)D_R \delta_{ij} \delta(t-t')$, and the rotational diffusion coefficient D_R .

The cognitive “visual” torque $\boldsymbol{M}_i^{\alpha\gamma}$ by particles of the same ($\gamma = \alpha$) or different ($\gamma = \beta$) type in the vision cone VC is [47, 48]

$$\boldsymbol{M}_i^{\alpha\gamma} = \frac{\Omega_{\alpha\gamma}}{N_{\alpha\gamma}} \sum_{j \in VC} e^{-r_{ij}^{\alpha\gamma}/R_0} \boldsymbol{e}_i^\alpha \times (\boldsymbol{u}_{ij}^{\alpha\gamma} \times \boldsymbol{e}_i^\alpha). \quad (4)$$

Here, $\boldsymbol{u}_{ij}^{\alpha\gamma} = \boldsymbol{r}_{ij}^{\alpha\gamma} / |\boldsymbol{r}_{ij}^{\alpha\gamma}|$ is the unit vector of the distance $\boldsymbol{r}_i^\alpha - \boldsymbol{r}_j^\gamma$ between particle i and j of the types α and γ , and

$$N_{\alpha\gamma} = \sum_{j \in VC} e^{-r_{ij}^{\alpha\gamma}/R_0} \quad (5)$$

is the normalization factor, which is determined by the effective number of such particles in the vision cone. The condition for particles j to lie within the vision cone of particle i is

$$\boldsymbol{u}_{ij}^{\alpha\gamma} \cdot \boldsymbol{e}_i^\alpha \geq \cos \theta_\alpha, \quad (6)$$

where θ_α – the vision angle – is the opening angle of the vision cone centered by the particle orientation $\boldsymbol{e}_{\alpha i}$, and R_0 describes the characteristic range of the visual perception. Additionally, the vision range is limited to

$$|\boldsymbol{r}_i^\alpha - \boldsymbol{r}_j^\gamma| \leq R_v, \quad (7)$$

treating all particles further apart than R_v as invisible ($R_v \geq R_0$). In a dilute system, only a single particle may be within the distance R_v , and the exponential factor $e^{-r_{ij}^{\alpha\gamma}/R_0}$ cancels out, as it appears both in the numerator and denominator in Eq. (4). Conversely, in a dense system, an effective reduced vision range R_0 appears due

to the exponential factor. This can be interpreted as blocking the view by neighboring particles highlighting the influence of the local environment on visual perception (similar to the effect studied in Ref. [5]).

The torque $\boldsymbol{M}_i^{\alpha\gamma}$ describes the preference of an iABP to move toward [44, 48] or away [56, 57] from the center of mass of iABPs of type γ in its vision cone VC , depending on the sign of the maneuverability $\Omega_{\alpha\gamma}$. The normalization Eq. (5) implies a nonadditive interaction, and emphasizes the importance of the effective particle number in the vision cone. It is motivated by the fact that additive and nonadditive interactions imply distinct macroscopic behaviors in interacting active systems [58].

We focus here on two-dimensional systems. Then, with the representation of the propulsion direction in polar coordinates, $\boldsymbol{e}_i^\alpha = (\cos \varphi_i^\alpha, \sin \varphi_i^\alpha)^T$ and the difference vector $\boldsymbol{u}_{ij}^{\alpha\beta} = (\cos \phi_{ij}^{\alpha\beta}, \sin \phi_{ij}^{\alpha\beta})^T$, Eq. (3) implies the equation of motion for the orientation angle φ_i^α

$$\dot{\varphi}_i^\alpha = \sum_{\gamma \in \{\alpha, \beta\}} \frac{\Omega_{\alpha\gamma}}{N_{\alpha\gamma}} \sum_{j \in VC} e^{-r_{ij}^{\alpha\gamma}/R_0} \sin(\phi_{ij}^{\alpha\gamma} - \varphi_i^\alpha) + \boldsymbol{\Lambda}_i(t), \quad (8)$$

with $\boldsymbol{\Lambda}_i$ a Gaussian and Markovian stochastic process of zero mean and $\langle \boldsymbol{\Lambda}_i(t) \cdot \boldsymbol{\Lambda}_j(t') \rangle = 2D_R \delta_{ij} \delta(t-t')$.

Although we consider a minimal model, the system contains a significant number of parameters, as there is the Péclet number $Pe = v_0 / (\sigma D_R)$ (where σ is the effective particle diameter) the vision angles θ_α ($\alpha \in \{A, B\}$), the vision range R_0 and cutoff radius R_v , the maneuverabilities $\Omega_{\alpha\beta}$, the packing fraction $\Phi = \pi \sigma^2 N / (4L^2)$ (with linear systems size L), and the particle numbers N_α , with $\alpha \in \{A, B\}$. This gives rise to a rich phase behavior and interesting dynamics.

B. Parameters

We measure lengths in units of the particle diameter σ , time in units of $\tau = \sqrt{m\sigma^2/(k_B T)}$, and energies in units of the thermal energy $k_B T$ [44, 48].

The friction coefficient γ_T is chosen as $\gamma_T = 10^2 \sqrt{mk_B T / \sigma^2}$, the rotational diffusion coefficient as $D_R = 8 \times 10^{-2} \sqrt{k_B T / (m\sigma^2)}$, which yields the relation $D_T / (\sigma^2 D_R) = 1/8$ with $D_T = k_B T / \gamma_T$. These choices ensure that inertia effects are negligible, since the small ratio $mD_R/\gamma = 8 \times 10^{-4} \ll 1$ implies a strongly over-damped single-particle dynamics [60]. The activity of the iABPs is characterized by the Péclet number

$$Pe = \frac{v_0}{\sigma D_R}. \quad (9)$$

The adaptation of the interaction strength $\epsilon/k_B T = (1 + Pe)$ warrants a nearly constant iABP overlap during iABP contacts, even at high activities [44]. Periodic boundary conditions are applied. The equations of motion (1) are integrated with a velocity-Verlet-based

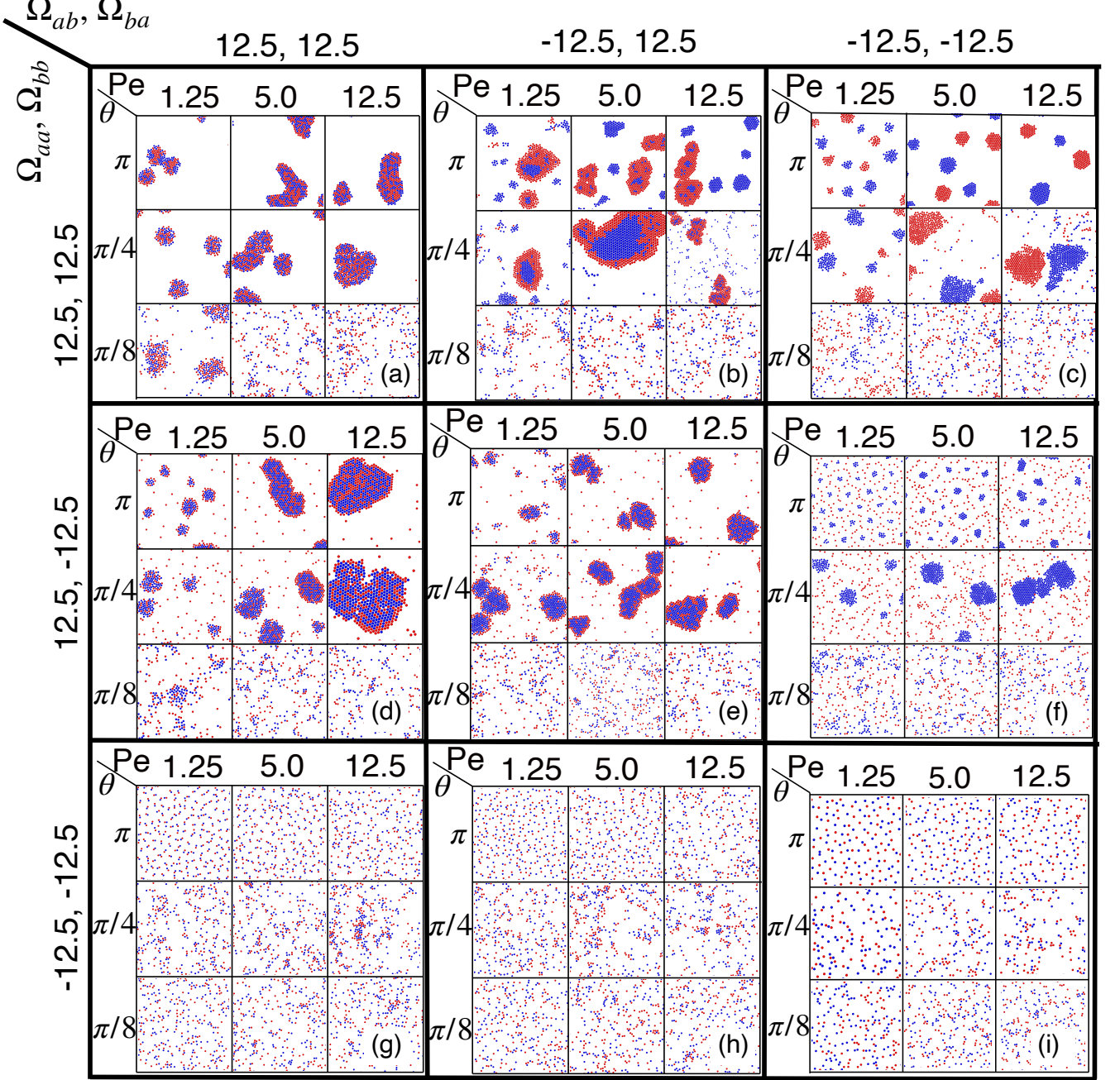


FIG. 2. Snapshots of phases for 9 combinations of the maneuverabilities and the Péclet numbers 1.25, 5.0, and 12.5, and vision angles π , $\pi/4$, and $\pi/8$. The number of particles is $N_A = N_B = N/2 = 500$ at the packing fraction $\Phi = 0.0785$. (See also Movie M1 [59].)

scheme suitable for stochastic systems [61], using the time step $\Delta t = 10^{-3}\tau$. The maneuverabilities $\Omega_{\alpha\beta}$ are scaled with D_R , such that $\Omega_{aa} = \Omega_{AA}/D_R$ etc. If not stated otherwise $R_0 = 1.5\sigma$ and $R_V = 4R_0$. Initially, the iABPs are typically arranged on a square lattice, with iABPs distances equal to their diameter σ , in the center of the simulation box.

We performed 10^7 relaxation steps, and collect data

for the subsequent 10^7 steps. For certain averages, up to 10 independent realizations are considered.

C. Phases and Phase Diagrams

Figure 2 presents an overview of emerging phases for nine combination of the maneuverabilities $\Omega_{\alpha\beta}$, with

equal magnitude and all possible sign combinations. In each case, the three Péclet numbers $Pe = 1.25, 5.0, 12.5$ and three vision angles $\theta_A = \theta_B = \theta = \pi, \pi/4, \pi/8$ are investigated. Various kinds of complex structures are obtained, such as mixed aggregates, segregated aggregates, layers of aggregates of one type of iABPs surrounded by a homogeneous layer of the other type of iABPs, homogeneous aggregates engulfed by the another type of iABPs, dimers, mixed states, and honeycomb lattice type structures.

In the following sections, the emerging structures and their dynamics will be discussed for several parameter combinations in more detail.

III. AVOIDING SAME, FAVORING OPPOSITE TYPE OF INTELLIGENT ABPS

A. Structures

A system, in which particles of the same type steer away and of opposite type steer toward each other, i.e. $\Omega_{aa} = \Omega_{bb} < 0$ and $\Omega_{ab} = \Omega_{ba} > 0$, bears some similarity with an electrostatic system, where equally charged particles repel and different charged particles attract. This analogy implies that the formation of “charge” dipoles (dimers) can be expected. Snapshots of the typical conformations are displayed for $\Omega_{aa} = \Omega_{bb} = -\Omega_0$ and $\Omega_{ab} = \Omega_{ba} = +\Omega_0$ with $\Omega_0 = 12.5$ in Fig. 2(g), and for $\Omega_0 = 62.5$ in Fig. 3. The emergent structures strongly depend on the vision angle and the Péclet number, as illustrated in Fig. 3(a) for equal particle numbers $N_A = N_B$. This reflects the nonreciprocal character of the vision interaction. For the small maneuverability $\Omega_0 = 12.5$ and low Pe , Fig. 2(g), as well as for $\Omega_0 = 62.5$ and all Pe , Fig. 3, hetero-dimers form for the large vision angle $\theta = \pi$, as for electrostatic interactions. Nevertheless, no dimer pairs, chains, or clusters are found, as might be expected from the electrostatic analogy. This is a consequence of the polarity of the iABPs by their propulsion direction, which breaks the spatial isotropy of their mutual interactions, although vision itself is isotropic and stabilizes dimers, but leads to a repulsive interaction between them, so that the average distance between dimers is determined by the number $N_A = N_B$ of iABPs. For a homogeneous spatial distribution of particles, the average distance d_p between dimers can be estimated from the density as $d_p = (4/\pi)^{1/2} (L^2/N_A)^{1/2} \approx 5\sigma$ (for $N = 1000$ and $L = 100$ as well as $N = 625$ and $L = 78.5$), in good agreement with simulation results. In contrast, for the small vision angle $\theta = \pi/16$, an iABP detects only other iABPs in a narrow vision cone – the spatial symmetry of vision is broken – and disordered structures of single particles are observed, especially for small Pe , as found in non-steering systems.

For vision angles $\pi/8$ and $\pi/4$, larger Péclet numbers, and the higher maneuverability $|\Omega_{\alpha\alpha}| = |\Omega_{\alpha\beta}| = 62.5$, self-organized patters appear, see Fig. 3(a). Even hexag-

onally close-packed structures are formed for large Pe . Specifically, double layers of similar iABPs reflect the nonreciprocal character of the interactions.

It is of course also interesting to consider non-stoichiometric systems, where one particle type, say A , is the minority component, i.e., $N_A < N_B$. Figure 3(b) illustrates the influence of the number ratio N_A/N_B at constant overall packing fraction on structure formation. Instead of A - B pairs, now clusters with a larger number of B -type iABPs appear. With increasing majority component B , clusters grow and several layers of B -type iABPs may form around A particles. The cluster size is limited by (i) the number of minority iABPs, and (ii) the vision range. For $\theta = \pi/4$ and $\pi/8$ and not too large ratios $N_B/N_A \approx 3$ and 7, similar layered structures of A - and B -type particles appear as for the stoichiometric case (at the same $Pe = 12.5$), although with a smaller number on A -type iABPs. For large vision angles $\theta \geq \pi/2$, the formation of triplets, septuplets, and larger aggregates is observed.

The (average) polarity field, determined by the orientation of the propulsion direction, in any cluster points preferentially toward a center of a cluster, although with some deviations in case of the opposite multilayers, see Fig. 3(a). In particular, the clusters in Fig. 3(b) for $N_A/N_B = 620/5$ and $\theta = \pi$ with a single central A -particle are very stable (see Movie M1). The B -type particles all point toward the central A particle, because the effective torque on a B particle by its neighboring B particles is close to zero, as (i) the torque on head-to-tail arranged particles with parallel propulsion direction is zero (see Eq. (4)), and (ii) the torque of the side-by-side arranged iABPs also nearly vanished due to their hexagonal arrangement. That leaves a residual preferred motion toward the A particle. Furthermore, the dispersed B particles in the gas phase surrounding a cluster repel those inside the cluster and thereby stabilize the phase separation.

B. Dynamics

To characterize the dynamical features of iABP self-organization, we consider their mean-square displacements (MSD)

$$\langle \mathbf{r}^2(t) \rangle = \frac{1}{N} \sum_{i=1}^N \langle (\mathbf{r}_i(t+t_0) - \mathbf{r}_i(t_0))^2 \rangle, \quad (10)$$

where the average is performed over the initial time t_0 . For vision angles $\theta \leq \pi/2$, the dynamics shows an ABP-like behavior, with a ballistic motion and a diffusive motion for times $D_R t \gtrsim 10$, see Fig. 4(a). To characterize the dynamics as a function of vision angle and Péclet number, we extract an effective translational diffusion coefficient D_L from the long-time MSD, as displayed in Fig. 4(b) as a function of the vision angle.

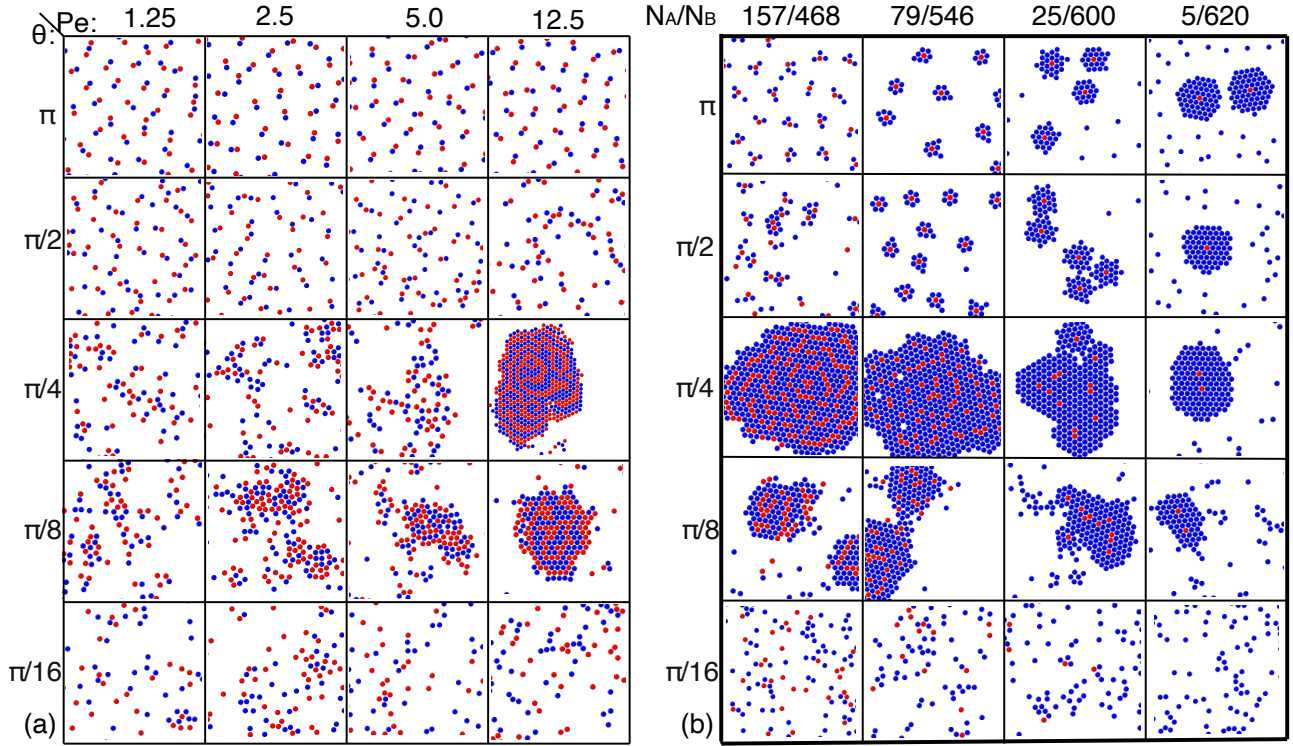


FIG. 3. Snapshot of phases for the maneuverabilites $\Omega_{aa} = \Omega_{bb} = -62.5$ and $\Omega_{ab} = \Omega_{ba} = 62.5$ and various combinations of (a) vision angle $\theta_A = \theta_B = \theta$ and Péclet number Pe for $N_B = N_A = 312$, and (b) and the ratio of the number N_A/N_B of the two types of iABPs and the vision angle for the Péclet number $Pe = 12.5$. The packing fraction is $\Phi = 0.0785$. (See also Movie M2 and M3 [59].)

For large vision angle $\theta = \pi$, the MSD is very small due to the formation of dimeric clusters. The self-propulsion of dimers is “screened”, because the propulsion directions point preferentially toward each other, as in a motility-induced phase separation of ABPs. In contrast to the latter, steering prevents a diffusive change of the propulsion direction and the pairs are stable for a long time.

At smaller vision angle $\theta = \pi/2$, dimers are less stable and the formed structures are more disordered, also larger temporary string-like (polymer-like) aggregates appear. The corresponding MSD is larger than that for $\theta = \pi$, but smaller than that for a non-steering ABP due to the formation of small clusters. Interestingly, an enhanced diffusion is also observed for the vision angles $\theta = \pi/4$ and $\pi/8$, which can be attributed to temporarily formed small clusters with highly inhomogeneous particle orientations, where the restricted rotational diffusion due to vision interaction causes a slightly enhanced persistent motion. Finally, at the very small vision angle $\theta = \pi/16$, where an iABP detects hardly any other iABPs, the system is in a disordered dilute phase, where the particles exhibit the same MSD as individual non-steering ABPs.

This behavior is of course also reflected in the results for the diffusion coefficient D_e . It first increases with increasing θ , then decreases for $\theta \gtrsim \pi/4$, as long as $Pe \lesssim 5.0$. In this range of Pe values, D_e is nearly independent of Pe , because motion is dominated by the

translational diffusion of dimers. For larger Péclet numbers, $Pe = 12.5$ and 25.0, large aggregates are present for $\theta = \pi/4$ and $\pi/8$ (compare Fig. 3(a)), where the total propulsion is reduced by partial compensation of the particle activity. The N_e “passivated” particles in the cluster diffuse with an effective diffusion coefficient $\sim 1/N_e$, which reduces the overall diffusion coefficient. Interestingly, D_e is larger for $Pe \leq 5.0$ and $\theta \leq \pi/2$ than for larger Pe , in particular for $Pe = 25.0$. This happens, because higher Pe stabilizes propulsion directions toward the cluster center. Finally, for $\theta = \pi/16$, the diffusion coefficients are well fitted by the relation $D_e = D_L/D_R \approx Pe^2 = v_0^2 \sigma^2 / (D_R^2)$ of non-steering ABPs.

The clusters in Fig. 3(a) for $\theta = \pi/4$ and $Pe = 12.5$, and those in Fig. 3(b) for $\theta = \pi$ and $N_A/N_B = 620/5$ exhibit an interesting collective dynamics. In the first case, a pronounced rotational motion appears due to a polarization of the propulsion directions. In the second case, the near-hexagonal arrangement of the B -type particles leads to a compensation of propulsion forces, and the cluster translates only very slowly with very little rotation.

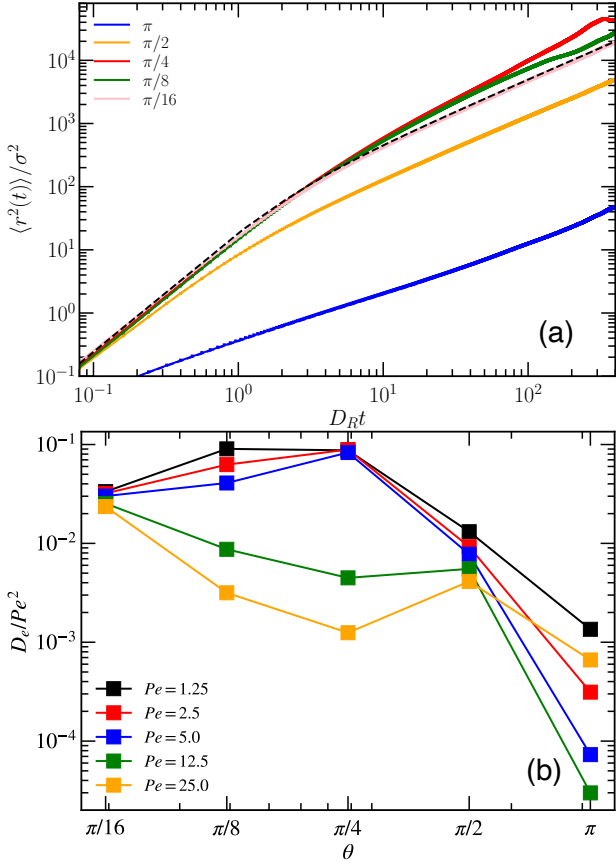


FIG. 4. Dynamics of iABPs. (a) Mean squared displacement (MSD) as a function of scaled time D_Rt for $Pe = 5.0$ and various vision angles θ . The black dashed line represents the MSD of non-steering ABPs. (Will (a) be removed?) (b) Effective diffusion coefficient $D_e = D_L/D_R$ extracted from the MSD, scaled by the square of the Péclet number, as a function of the vision angle θ for various Pe . The number ratio is $N_B/N_A = 312/313$, the packing fraction is 0.0785.

C. Hopping

In the nearly stoichiometric case, with $N_B = N_A + N_d$ and $N_d \ll N_A$, A - B dimers dominate in the conformations but are accompanied by N_d unpaired iABPs. These unpaired particles can shuttle between dimers and exchange places with particles within the dimers. Hence, we denote such an unpaired particle as a hopper in the following. The transport of unpaired particles resembles the Grotthuss mechanism of proton transport from one water molecule to another via the formation and breaking of hydrogen bonds [62]. However, the transport of hoppers between dimers is by active motion and not by hydrogen bond rearrangements along a network, as in the Grotthuss mechanism [62].

Figure 5 shows sequences of such hopping events, where a particle from a pair is replaced by a hopper, resulting in the formation of a new pair. To define a hopper, we use a distance criterion – as long as a particle

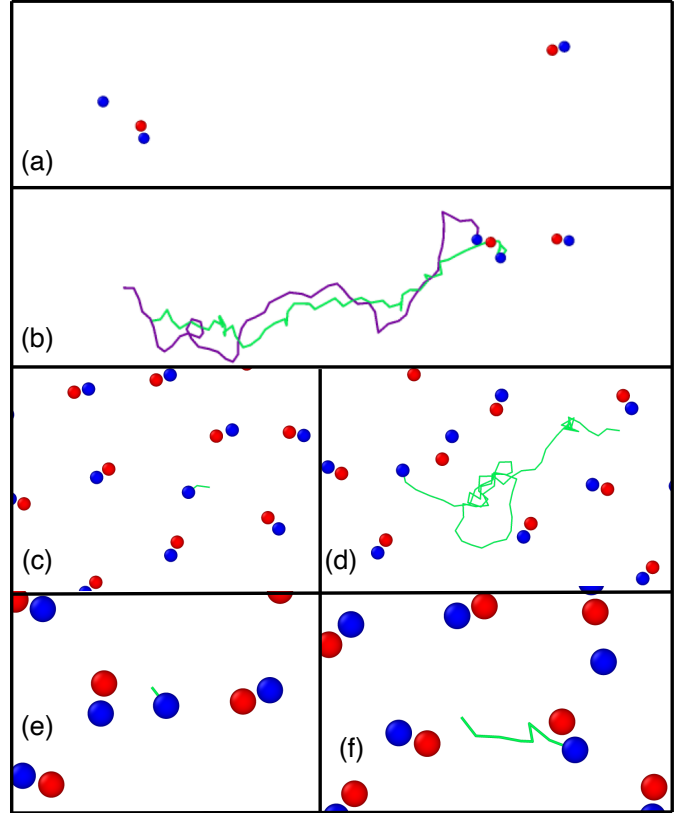


FIG. 5. Snapshots of the hopper-pair exchange dynamics. The depicted sequences illustrate the replacement of a particle within a pair by a “hopper”, leading to the formation of a new hopper. Initially (a), (c), (e) a blue hopper, steers toward the red particle of a pair at the packing fractions (a), (b) $\Phi = 0.00785$, (c), (d) $\Phi = 0.03925$, and (e), (f) $\Phi = 0.0785$. (b), (d), (f) Subsequently to an exchange, a blue hopper traverse the green trajectory and substitutes another blue particle within the pair. The parameters used are $N_d = 5$ and $Pe = 12.5$. (See Movie M4 [59].)

is not within the distance $h_d = 1.5\sigma$ of another particle, it is a hopper. The dynamics of hoppers depends on the Péclet number, the packing fraction, and the number $N_d = |N_B - N_A|$ of excess B - or A -type particles beyond stoichiometry.

1. Hopper number, encounter distance, displacement, and hopping time

Figures 6(a) and (b) show the average number N_{hopp} of hoppers present in the system at various activities and packing fractions. Interestingly, at small $Pe = 1.25$ the number of hoppers is larger compared to higher Pe , and increases only slightly as the number difference N_d increases. This larger number N_{hopp} is due to thermal noise. Despite opposite-type particles steering toward each other, noise disrupts their sustained proximity, and suppresses long-time stable pair formation, which results

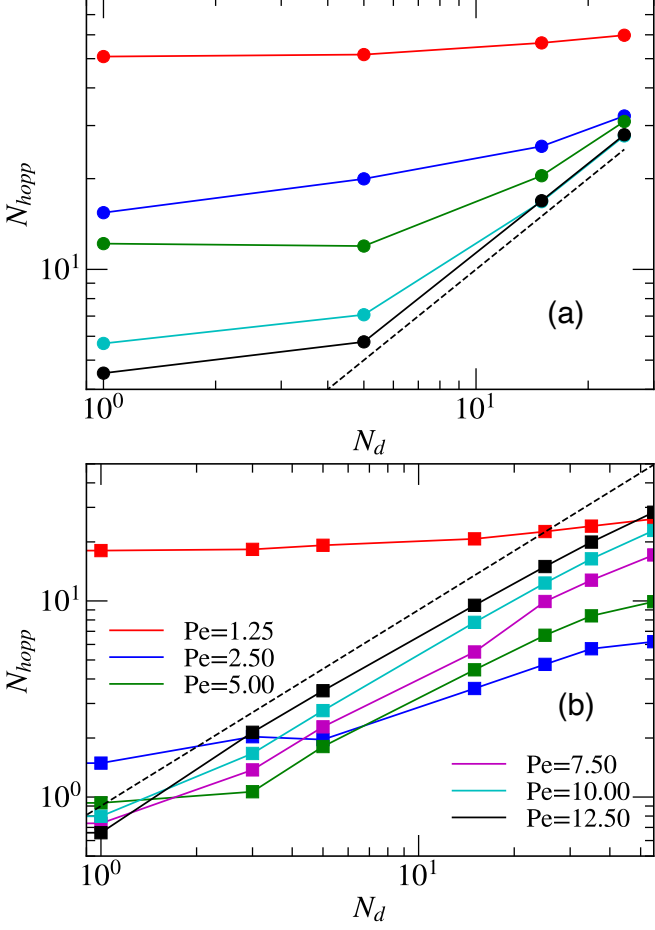


FIG. 6. Activity dependence of the number of hoppers. Number N_{hopp} of hoppers as a function of the number difference $N_d = N_B - N_A$ for various Péclet numbers (Pe) and the packing fractions (a) $\Phi = 0.00785$ and (b) $\Phi = 0.0785$. The dashed lines correspond to $N_{hopp} = N_d$.

in the creation of many hoppers. At the low density $\Phi = 0.00785$ (Fig. 6(a)), the number of hoppers decreases with increasing activity, as dimers become more stable. N_{hopp} decreases with increasing packing fraction at fixed Pe and N_d , as the distance between dimers decreases and they become less susceptible to a particle exchange (see Figs. 6(a) and (b)). For the higher packing fraction $\Phi = 0.0785$ (Fig. 6(b)), N_{hopp} is smaller than for the lower packing fraction (Fig. 6(a)) (at a given Pe and N_d). Due to the larger density, hoppers are more likely to meet dimers, but the exchange process takes longer, which results in more stable clusters of three particles and, hence, a reduced number of hoppers. At large Pe and N_d – the latter number depends on the packing fraction – N_{hopp} increases approximately linearly with the number difference, which suggest that approximately all minority-type A particles are bound in pairs.

To further characterize the hopping behavior in the process of the formation of a new pair, we calculate the average hopping time Δt and the average hopping dis-

placement $|\Delta\mathbf{r}|$. The results presented in Fig. 7 reflect a distinct density dependence. For higher packing fractions, hoppers traverse small distance only and thus have a high encounter probability with A - B pairs or other free particles, which expedites the of hopper-transfer process. Conversely, for lower packing fraction, the hopping times increase similar to the increasing traversed distances. The shortest average hopping time occurs at Péclet number $Pe = 1.25$, again due to the dominance of noise. As particles in a pair are loosely attached to each other, hoppers can easily break a pair and generate a new pair and a new hopper. As the activity increases ($Pe \lesssim 5.0$), dimers are more stable and the hopping time increases. For even larger Pe , $D_R\Delta t$ is almost constant or decreases with in increasing Pe , depending on density, due to the enhanced persistent motion of the iABPs.

The simulation results for the hopping time Δt suggest that it is mainly determined by the distance a hopper covers before exchanging with another pair, see Fig. 7(a). This is different for the displacement $|\Delta\mathbf{r}|$ displayed in Fig. 7(b), which scales very well with the average dimer distance $1/\sqrt{\rho}$, and increases monotonically with increasing Péclet number and saturates for large Pe . Notably, $|\Delta\mathbf{r}|$ is very similar for the largest and smallest considered packing fraction. Moreover, the two quantities presented in Figs 7(a) and (b) are independent of the number difference for packing fraction $\Phi = 0.0785$ and $\Phi = 0.00785$.

Remarkably, the systems at the intermediate packing fraction $\Phi = 0.03925$ exhibit a different behavior. First, the average hopping time depends on the number difference. Second, the maximum average hopping time is larger than the values for the larger and smaller packing fractions. We conjecture that this is related to collective effects. At this intermediate density, hoppers are typically equidistant from other pairs, hence selection and motion toward the closest dimer is ambiguous. In addition, pairs are more responsive to an approaching hopper compared to higher density systems. Thus, a hopper requires a longer time to reach a dimer and replace a paired iABP.

2. Mean-Square Displacement: Caging and Chasing

To characterize the dynamics of iABPs in the "hopping phase", we evaluate the mean-square displacement (MSD) of the A and B particles. The characterization of the dynamics of hoppers itself is only possible for rather short times due to frequent recombination and exchange with A - B pairs. The presence of the majority B component affects the dynamics of the mixture. Depending on the parameters, we find short- and intermediate-time regimes with sub- and super-diffusive behavior – the long-time dynamics (with $D_R t \gtrsim 40$) is always diffusive. The various MSD regimes are differentiated by their power-law time dependent MSD $t^{\alpha_{1,2}}$, with exponents α_1 in the short-time ($D_R t < 2$) and α_2 in the intermediate-time

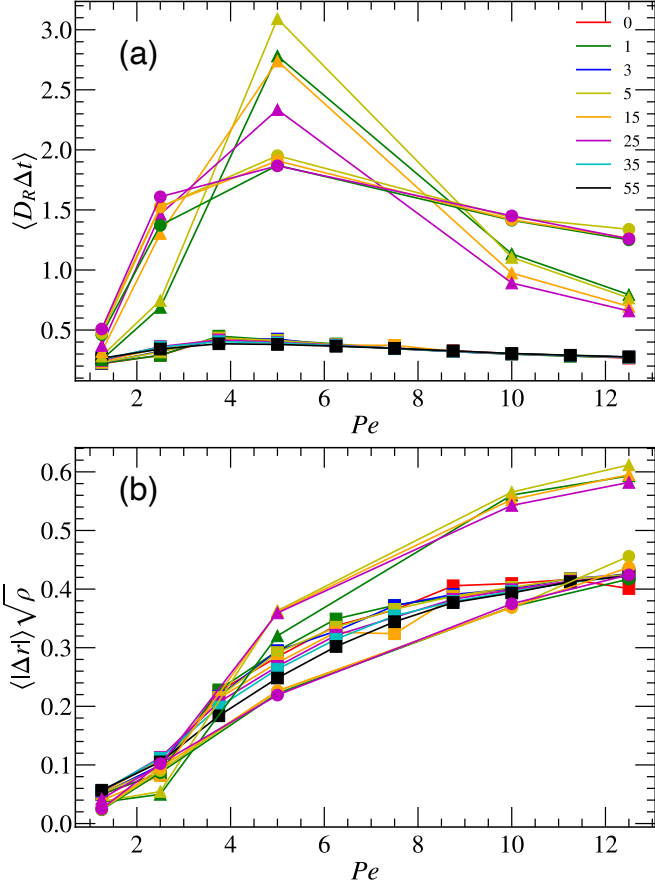


FIG. 7. Characteristic average life times and displacements of hoppers as a function of Péclet number and for various number differences N_d (legend). (a) Average hopping time $\langle D_R \Delta t \rangle$, during which a hopper is unbound before combining with other particles, and (b) average scaled displacement $\langle |\Delta r| \rangle \sqrt{\rho}$ as a function of the Péclet number Pe for various number difference N_d (see legend). Here, $\rho = (N_A + N_B)/L^2$ is the number density of iABPs. Packing fractions are indicated by different symbols, with $\Phi = 0.0785$ (squares), 0.03925 (triangles), and 0.00785 (bullets).

($2 < D_R t < 20$) regime.

Figures 8(a) and (b) show values of the exponent $\alpha_{1,A}$ of A (minority) and $\alpha_{1,B}$ of B (majority) particles for the large packing fraction $\Phi = 0.0785$. The values $\alpha_{1,A} < 1$ (see Fig. 8(a)) reflect a subdiffusive nature of the minority A particles, which are typically paired with B particles, which repel other B particles and thus exhibit a caging effect (see Figs. 2(g), 3(b)). The exponent $\alpha_{1,A}$ decreases with increasing activity as the propulsion directions in these dimeric pairs are more strongly aligned toward each other, which reduces the overall (active) dynamics. The weak dependency on N_d , with the lowest value of $\alpha_{1,A}$ at large $N_d = 55$ and the highest at low $N_d = 1$, can be attributed to the fact that the larger the number difference the smaller is the long-time stability and mobility of individual dimers.

The majority B -type iABPs exhibit nearly diffusive

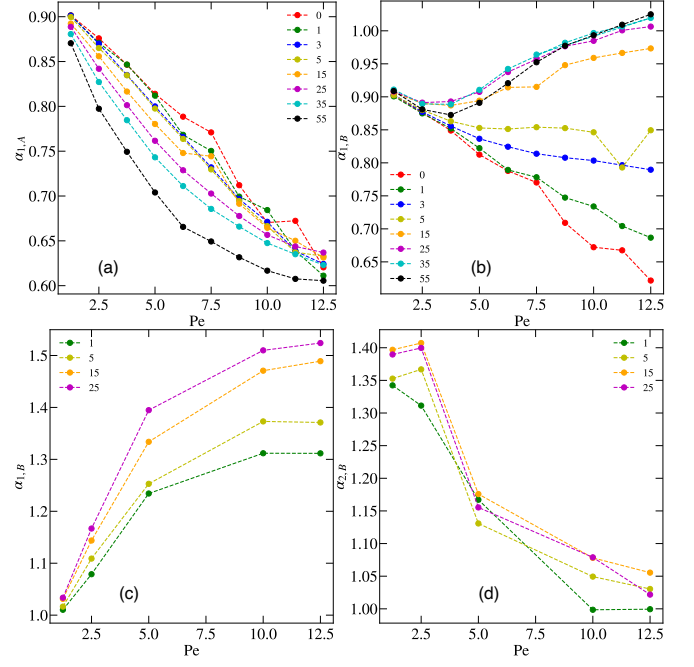


FIG. 8. Dynamics of A - and B -type iABPs, characterized by the MSD exponent $MSD \sim t^\alpha$ for the short and intermediate time range. (a) Exponents $\alpha_{1,A}$ for A (minority) particles and (b) $\alpha_{1,B}$ for B (majority) particles at the packing fraction $\Phi = 0.0785$; (c) exponents $\alpha_{1,B}$ and (d) $\alpha_{2,B}$ for B particles as a function of the Péclet number Pe and various N_d (legend). The total number of particles is $N = N_A + N_B = 625$.

behavior for $N_d \lesssim 5$ and $Pe < 2.5$ (see Fig. 8(b)). However, the exponent $\alpha_{1,B}$ decreases with increasing Pe . This is a consequence of the more stable A - B pairs at larger Pe , which leads to a drop in the number of (highly mobile) hoppers (see Fig. 6). The A and B particles exhibit then a similar, cage-determined diffusive behavior (cf. Fig. 8(b)). With increasing N_d , more free hoppers are present (Fig. 6) and $\alpha_{1,B}$ increases, approaching the diffusion limit $\alpha_{1,B} = 1$ for $N_d \gtrsim 15$, nearly independent of the Péclet number.

The dynamics of the iABPs is rather different in the dilute systems with packing fraction $\Phi = 0.00785$. The minority A particles are as mobile as the B particles, consequently the values of the exponents are $\alpha_{1,B} \approx \alpha_{1,A}$ and $\alpha_{2,B} \approx \alpha_{2,A}$. In fact, the MSD is smaller for B s than for A s, because the opposing propulsion directions in pairs reduce the activity contribution to their dynamics. Propulsion implies a super-diffusive dynamics at short and intermediate time scales, with exponents $\alpha_{1,B} > 1$ (for $Pe > 2.5$) and $\alpha_{2,B} > 1$ (for $Pe < 10.0$), where an increasing activity leads to an increasing exponent at short times (see Fig. 8(c)) and a decreasing exponent for intermediate times (see Fig. 8(d)). The growth of the exponent $\alpha_{1,B}$ can be attributed to an enhanced mobility of the iABPs by the increasing activity, in analogy to that of active Brownian particles. Interestingly, hoppers can chase A - B pairs (compare Fig. 5), in which the

propulsion directions turn approximately in the same direction, hence, leads to an enhanced dynamics of the hopper and the pair. As N_d increases, the number of hoppers which chase a pair increases, thus, the effective mobility of both increases too, which is reflected in a growth of the exponent $\alpha_{1,B}$ with increasing N_d . In the intermediate time regime, $2 < D_{Rt} < 20$, hoppers are super-diffusive at small Péclet numbers. This is explained by an activity-enhanced dynamics as in the short-time regime for large Pe . With increasing Pe , the activity-enhanced time regime shifts to shorter times, and in the intermediate regime hoppers exhibit the long-time diffusive behavior, which is only weakly dependent on the number difference N_d .

IV. PREDATOR-PREY BEHAVIOR

When like-particles attract each other, while A particles chase B particles, which try to escape from A particles – with maneuverabilities $\Omega_{aa} = \Omega_{bb} = +\Omega_0$, and $\Omega_{ab} = -\Omega_{ba} = \Omega_0$ – a predator-prey-type of collective behavior is observed. This combination of the signs of maneuverabilities leads to the formation of cohesive groups and clusters by the same kind of particles (compare Fig. 2(b)). We consider here a system, where the vision angles of the two particle types are *not* the same, but a narrow vision angle $\theta_A = \pi/4$ for the predator, and a large vision angle $\theta_B = \pi$ for the prey. Note that throughout this simulation study we consider the case where the Péclet number is the same for A and B particles, so that the speeds of predator and prey are the same! The emerging clusters can be considered as “hunting packs” of type- A particles chasing “herds” of prey-like type- B particles. Figure 9 displays a sequence of snapshots illustrating a typical pursuit scenario (see also Movie M5). Clearly, the prey particles form various coexisting clusters, while the number of predator particles is too small for the formation of larger clusters. As time moves on, the predator approaches a prey cluster, and the prey particles try to escape, while the predator maintains its moving direction until the prey cluster has dispersed and the predator encounters another prey cluster.

The spatial distribution of prey particles around a predator is displayed Fig. 10 for various maneuverabilities $|\Omega_{ab}|$, averaged over several encounters of predator and prey. The distribution of prey is symmetric in the direction perpendicular to the predator’s moving direction and asymmetric along the propulsion direction, with a depletion of the number of prey particles behind the predator. As the prey senses the predator, it steers away from it. Since the small vision angle of the predator, $\theta_A = \pi/4$, provides only a limited view on the prey and its steering maneuverability, $|\Omega_{ab}| = 12.5$, is low, the predator moves toward the prey in front, and most of the prey can escape sidewise and keep at a reasonable distance of approximately 4.5σ from the predator. How-

ever, when the predator’s steering maneuverability is increased to $|\Omega_{ab}| = 100$, the predator can catch up with the prey more easily, and move closer to the prey.

A quantitative characterization of the prey distribution in the moving direction of the predator is shown in Fig. 11 for various vision angles θ_A (Fig. 11(a)) and maneuverabilities $|\Omega_{ab}|$ (Fig. 11(b)). As a predator moves closer to a group of prey, prey particles sensing the predator disperse first by moving sidewise and reconvene later. Due to the cohesion of the prey cluster, even prey particles outside of the vision range of the predator move away from it and become depleted in its vicinity. Hence, the number of prey particles is drastically reduced behind the predator ($x \leq 0$). Conversely, in front of the predator, there is a substantial accumulation of prey that the predator is actively steering toward. For smaller predator vision angles, such as $\pi/16$, the visual field is narrower, leading to a reduced prey detection and subsequently lower prey densities. As θ_A increases to $\pi/8$ and $\pi/4$, the prey density reaches its maximum in front of the predator. A further increase of θ_A to $\pi/2$ and π leads again to a decline of the prey density. Hence, the optimal vision angle of a predator to hunt prey lies around $\pi/4$, which provides focused vision (“eagle’s eye”). The broader field of view for $\theta_A \geq \pi/2$ counteracts effective steering toward prey, because the visibility of prey in many different directions implies a less goal-oriented and more erratic motion of the predator.

Figure 11(b) illustrates the prey’s number distribution around the predator for the angle $\theta_A = \pi/4$ and various maneuverabilities $|\Omega_{ab}|$. Again, an asymmetric distribution evolves, which is characterized by the scarcity of prey behind the predator and an accumulation in front. At large predator maneuverability, $|\Omega_{ab}| = 200$, the probability for the predator to encounter a large number of prey particles in close proximity is high, because the predator can rapidly adjust its orientation and direction of movement, optimizing its chance of closely approaching and catching the prey. This probability diminishes as the maneuverability $|\Omega_{ab}|$ decreases, as the predator struggles to efficiently position itself in relation to the prey, resulting in a reduced likelihood of the predator to closely approach the prey.

V. HONEYCOMB-LATTICE-TYPE STRUCTURE FORMATION

We want to illustrate the enormous variability of self-organization in mixtures of self-steering active agents by briefly discussing another intriguing phase, a quasi-periodic lattice structure, honeycomb-like lattice. Such a phase is obtained when one particle type (B) wants to aggregate, the other (A) to disperse, while different types want to avoid each other. This happens for the maneuverabilities $\Omega_{aa} = -\Omega_{bb} < 0$, and $\Omega_{ab} = \Omega_{ba} < 0$. Figure 12 displays snapshots for $N_A = N_B$, which reflect the dependence of the emerging lattice on the vision cut-

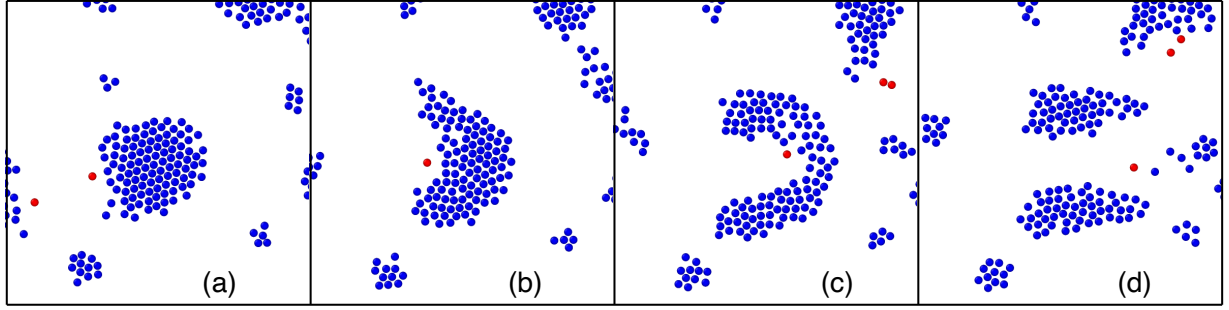


FIG. 9. Snapshots of a predator-prey pursuit. Series of snapshots (zoomed) progressing in time from (a)-(d), which illustrate a typical pursuit of a predator (red) chasing prey particles (blue). The parameters are $N_B/N_A = 50/1$, $\theta_A = \pi/4$, $\theta_B = \pi$, $\Omega_{aa} = \Omega_{bb} = 12.5$, $\Omega_{ab} = 12.5$, $\Omega_{ba} = -12.5$, and the number of particles $N_A + N_B = 1000$. (See also Movie M5 [59].)

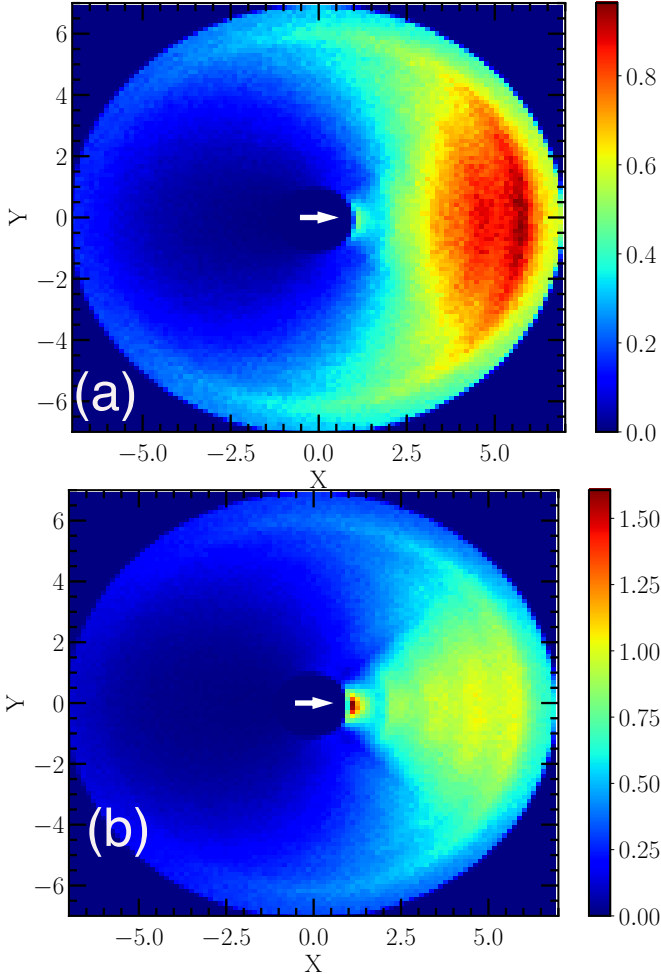


FIG. 10. Distribution of the number of prey particles around a predator for the maneuverabilities (a) $\Omega_{ab} = 12.5$ and (b) $\Omega_{ab} = 50$. The white arrow in the center indicates the predator's moving direction. The other parameters are $\Omega_{aa} = \Omega_{bb} = 12.5$, $\Omega_{ba} = -12.5$, $Pe = 1.25$, $\theta_A = \pi/4$, $\theta_B = \pi$, $N_B/N_A = 50/1$, and $N_A + N_B = 1000$.

off range R_v (see also Fig. 2(f)). When the vision cutoff range is small (Fig. 12(a), $R_v = 4.0\sigma$), particle segregation is weak, only small clusters form and locally diffuse honeycomb-like structures occur. As the vision range increases to $R_v = 14.0\sigma$ (Fig. 12(b)), a pronounced and well-defined honeycomb lattice is formed. This extension of the cut-off range increases the number of particles in specific areas, the lattice structure becomes better defined, and a noticeable number of particles cluster together in the center of each hexagon as well as along its edges. Thus, the visual interaction range can play a crucial role in the formation of particular structures of iABPs.

Figure 13(a) displays the pair correlation-function for B particles, which demonstrates the prevalence of the honeycomb lattice structures. At small R_v , small cluster of B particles are formed and a fluid-like distribution appears at distances $r/\sigma > 5$. With increasing R_v , the core clusters grows with pronounced peaks at the various B particle layers. In addition, a broad peak grows and shifts to larger distances with increasing R_v , indicating the position of the first hexagonal shell of neighboring B particle clusters, where its width accounts for the average number of B particles in the respective clusters.

It is also interesting to consider the dynamics of the structure formation of the honeycomb lattices. Starting from a uniform distribution of iABPs, we determine the average size of B clusters and their growth for the various cut-off radii R_v . A particle is considered part of a cluster if the distance with another particle in the cluster is $r \leq 1.5\sigma$. Figure 13(b) illustrates the average cluster growth. At short times $D_R t < 0.1$, all systems exhibit a similar behavior independent of R_v . However, for longer times $D_R t > 1$, clusters are formed, which grow with time until they reach a stationary state. For the cut-off range $R_v = 4\sigma$, the average cluster contains about four particles and there are many clusters (Fig. 12(a)). The clusters are very dynamic and reform continuously. The cluster size gradually increases with increasing vision cutoff range, reaching approximately 30 iABPs for $R_v = 14\sigma$. It is important to note that the coarsening effectively stops because the A particles in the hexagon

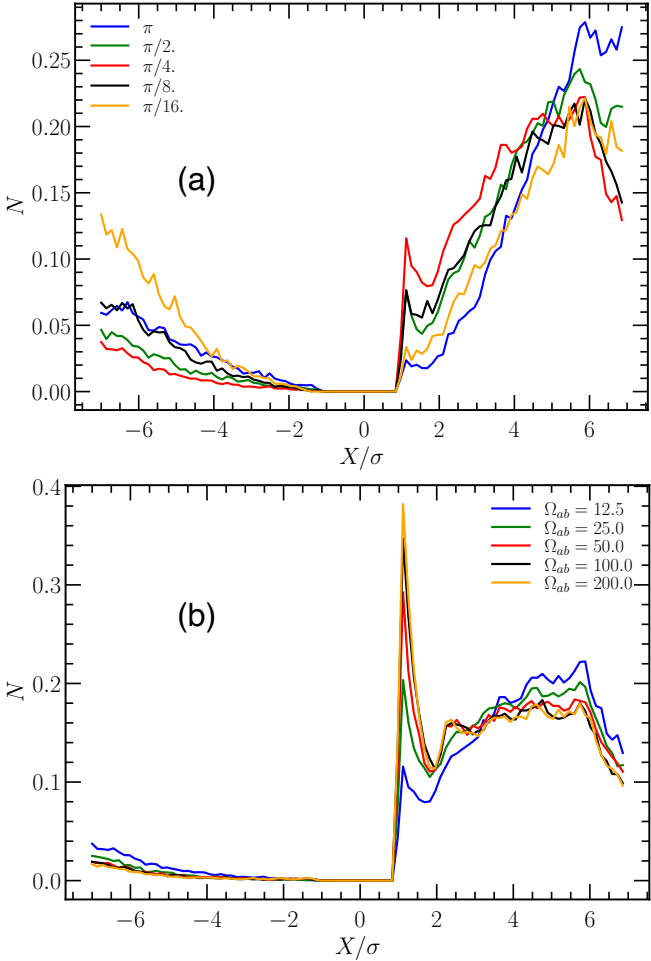


FIG. 11. Number of prey particles (B) in the direction of motion of the predator (A) for (a) various vision angles θ_A and $\Omega_{ab} = 12.5$, and (b) various maneuverabilities and $\theta_A = \pi/4$. The other parameters are the same as in Fig. 9.

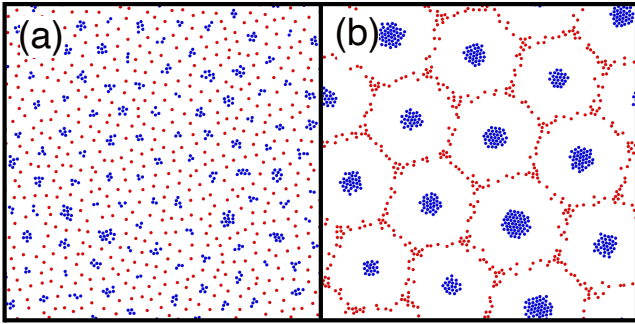


FIG. 12. Snapshots of honeycomb-type lattices. The various structures follow by varying the vision range R_v , where in (a) $R_v = 4.0\sigma$, and (b) $R_v = 14.0\sigma$. The maneuverabilities are $\Omega_{aa} = -12.5$, $\Omega_{aa} = 12.5$, $\Omega_{ab} = \Omega_{ba} = -12.5$. Furthermore, $Pe = 1.25$, $N_A + N_B = 1000$, $\theta_A = \theta_B = \pi$, and $\Phi = 0.0785$. (See also Movie M6 [59].)

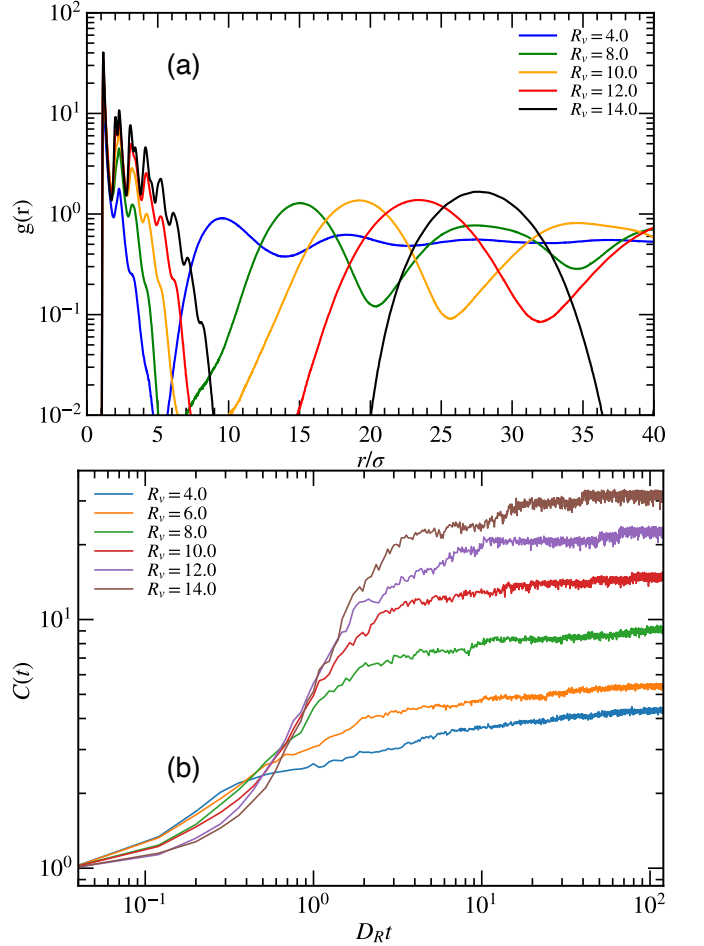


FIG. 13. (a) Pair correlation-function of B particles as a function of the radial distance for various vision cutoff radii R_v (legend). (b) Average number $C(t)$ of B iABPs in a cluster as a function of the scaled time $D_R \Delta t$ for various vision cutoff radii R_v . The Péclet number is $Pe = 1.25$. The other parameters are the same as in Fig. 12.

boundaries present an efficient barrier for the crossing of B particles. Thus, the hexagonal structure is very stable despite its dynamic nature.

VI. SUMMARY AND CONCLUSIONS

We have studied binary mixtures of self-steering active particles, where particle motion and steering is based on the instantaneous position of neighboring particles using a minimal cognitive model. The particle speed, vision angle, vision range, and sign and strength of maneuverability – relative to their peers and the foreign species – all play crucial roles in the self-organization and structure formation. Beyond a general overview of the enormous variability of emerging structures, we focus on the dynamical properties of three interesting self-organized phases, multimeric aggregates in off-stoichiometric mixtures, prey-predator-type behavior, and the formation of

honeycomb-type lattices.

In the case of steering properties reminiscent of systems with electrostatic interactions, the number ratio of the two components plays a crucial role in structure formation, along with vision angle and activity, which leads to the emergence of dimers, tetramers, and higher multimeric aggregates. For particle numbers which deviate slightly from stoichiometric ratios, unpaired particle display a hopping dynamics between multimers, where they can knock out a particle in the existing aggregate and substitute it, resulting in a sub-diffusive (caged) behavior at short times and diffusing motion at a longer time. The analysis of the mean hopping displacement shows a strong density dependence, where a high/low-density system has the smallest/highest hopping displacement.

In the case of a nonreciprocal steering response between the two particle types, i.e. $\Omega_{ab} = -\Omega_{ba}$, and only one of the types (the “prey”) preferring the vicinity of their peers, the emergent dynamics displays a predator-prey-like behavior. Our analysis reveals that the optimal angle for the predator to steer toward the prey is around $\pi/4$, corresponding to focused vision, which allows the predator to steer effectively toward the prey without getting distracted to much by other prey. Our simulation results are strikingly similar to the behavior of some natural systems, like reef shark in a fish swarm [63]; this type of predator-prey behavior has actually already been employed [64] to construct congestion avoidance for multiple micro-robots. Our results should provide the necessary guidance to optimize the design of such micro-robotic systems.

Finally, we considered a similar case with nonreciprocal A - B interactions as before, but now its only the predators which look for the vicinity of their peers. This seemingly small change generated a completely different kind of self-organization, where predator clusters to form a very stable honeycomb lattice with the vision cutoff range determining the size of the cluster and the lattice constant – with larger clusters for larger vision range.

Our system displays some fundamental and phenomenological similarities with mixtures of chemically interacting particles, which produce or consume a chemical to which they are attracted or repelled [52]. In both cases, nonequilibrium nonreciprocal interactions between particles, which break action-reaction symmetry lead to new classes of active phase separation phenomena. For example, the formation of molecule-like binary aggregates, and of honeycomb-like lattices are observed in both systems. However, a closer look reveals also several

important differences. First, interactions in the chemical system are isotropic, while our iABPs have directed sensing through the vision cone with a limited vision angle. Secondly, motion in the chemical systems develops as a results of chemotactic motion, while ABPs move with constant speed; the latter implies that iABPs can only react to gathered information by steering, for which we impose a limited maneuverability. These differences imply strikingly different emergent structure formation and dynamics. For example, hopping “defects” in the phase of small molecule-like aggregates in only seen for iABPs, as well as the animal-like predator-prey behavior. In contrast, static cluster of one particle type propelled by corona and tail of the other particle type are only seen in the chemical system.

A important advantage of our “minimalist” model of binary cognitive particle mixtures is its flexibility, which facilitates the description of a large variety of natural [65] and artificial [64, 66] systems. Here, (micro)robotic systems are very promising experimental model systems, as they allow the implementation of many different, simple or complex, interaction and steering rules. For example, a recent study [66] of a binary systems of programmable robots with non-reciprocal interactions, where species A aligns with B but B antialigns with A demonstrates the emergence of a collective chiral motion that can be stabilized by limiting the robot angular speed to be below a threshold. It will also be interesting to explore and utilize possible synergies between agent-based models and Cahn-Hilliard-type continuum field theoretical approaches [67–69] to elucidate the behavior of nonreciprocal multi-component systems.

Thus, the extension of single-component cognitive active particle systems to nonequilibrium two-component mixtures with nonreciprocal interactions generates an enormous richness of emergent complexity and variability of self-organization and dynamical scenarios. Despite of several recent studies, the large space of of self-organization behavior has just been scratched at the surface so far, and more detailed studies to elucidate the underlying physical mechanisms are required.

DATA AVAILABILITY

The data that support the findings of this paper are openly available [70].

[1] H. C. Berg, Bacterial behaviour, *Nature* **254**, 389 (1975).
 [2] A. Be’er, B. Ilkanaiv, R. Gross, D. B. Kearns, S. Heidenreich, M. Bär, and G. Ariel, A phase diagram for bacterial swarming, *Commun. Phys.* **3**, 66 (2020).
 [3] I. S. Aranson, Bacterial active matter, *Rep. Prog. Phys.* **85**, 076601 (2022).
 [4] A. Cavagna and I. Giardina, Bird flocks as condensed matter, *Annu. Rev. Cond. Mat. Phys.* **5**, 183 (2014).
 [5] D. J. Pearce, A. M. Miller, G. Rowlands, and M. S. Turner, Role of projection in the control of bird flocks, *Proc. Natl. Acad. Sci. USA* **111**, 10422 (2014).

[6] T. Vicsek, A. Czirók, E. Ben-Jacob, I. Cohen, and O. Shochet, Novel type of phase transition in a system of self-driven particles, *Phys. Rev. Lett.* **75**, 1226 (1995).

[7] J. Elgeti, R. G. Winkler, and G. Gompper, Physics of microswimmers—single particle motion and collective behavior: a review, *Rep. Prog. Phys.* **78**, 056601 (2015).

[8] C. Bechinger, R. Di Leonardo, H. Löwen, C. Reichhardt, G. Volpe, and G. Volpe, Active particles in complex and crowded environments, *Rev. Mod. Phys.* **88**, 045006 (2016).

[9] G. Gompper *et al.*, The 2020 motile active matter roadmap, *J. Phys. Condens. Matter* **32**, 193001 (2020).

[10] G. Gompper *et al.*, The 2025 motile active matter roadmap, *J. Phys. Condens. Matter* **37**, 143501 (2025).

[11] B.-W. Park, J. Zhuang, O. Yasa, and M. Sitti, Multifunctional bacteria-driven microswimmers for targeted active drug delivery, *ACS nano* **11**, 8910 (2017).

[12] T. Bäuerle, A. Fischer, T. Speck, and C. Bechinger, Self-organization of active particles by quorum sensing rules, *Nat. Commun.* **9**, 1 (2018).

[13] J. Bastos-Arrieta, A. Revilla-Guarinos, W. E. Uspal, and J. Simmchen, Bacterial biohybrid microswimmers, *Front. Robot. AI* **5**, 97 (2018).

[14] S. Yan, X. Zeng, Y. Wang, and B.-F. Liu, Biomaterialization of bacteria by a metal–organic framework for therapeutic delivery, *Adv. Healthc. Mater.* **9**, 2000046 (2020).

[15] M. Sitti, H. Ceylan, W. Hu, J. Giltinan, M. Turan, S. Yim, and E. Diller, Biomedical applications of untethered mobile milli/microrobots, *Proc. IEEE* **103**, 205 (2015).

[16] Y. Fu, H. Yu, X. Zhang, P. Malgaretti, V. Kishore, and W. Wang, Microscopic swarms: From active matter physics to biomedical and environmental applications, *Micromachines* **13**, 295 (2022).

[17] J. Hu, S. Zhou, Y. Sun, X. Fang, and L. Wu, Fabrication, properties and applications of janus particles, *Chem. Soc. Rev.* **41**, 4356 (2012).

[18] Z. You, A. Baskaran, and M. C. Marchetti, Nonreciprocity as a generic route to traveling states, *Proc. Natl. Acad. Sci.* **117**, 19767 (2020).

[19] S. Saha, J. Agudo-Canalejo, and R. Golestanian, Scalar active mixtures: The nonreciprocal cahn-hilliard model, *Phys. Rev. X* **10**, 041009 (2020).

[20] S. Osat and R. Golestanian, Non-reciprocal multifarious self-organization, *Nat. Nanotechnol.* **18**, 79 (2023).

[21] C. H. Meredith, P. G. Moerman, J. Groenewold, Y.-J. Chiu, W. K. Kegel, A. van Blaaderen, and L. D. Zarzar, Predator–prey interactions between droplets driven by non-reciprocal oil exchange, *Nat. Chem.* **12**, 1136 (2020).

[22] G. Natan, V. M. Wrolitzer, G. Ariel, and A. Be'er, Mixed-species bacterial swarms show an interplay of mixing and segregation across scales, *Sci. Rep.* **12**, 16500 (2022).

[23] Q. Wang, J. G. Frye, M. McClelland, and R. M. Harshey, Gene expression patterns during swarming in salmonella typhimurium: genes specific to surface growth and putative new motility and pathogenicity genes, *Mol. Microbiol.* **52**, 169 (2004).

[24] S. E. Burriel and R. Colin, Active density fluctuations in bacterial binary mixtures, *bioRxiv* , 2023 (2023).

[25] B.-L. Tang *et al.*, A predator-prey interaction between a marine *pseudoalteromonas* sp. and gram-positive bacteria, *Nat. Commun.* **11**, 285 (2018).

[26] J. R. Seymour, D. R. Brumley, R. Stocker, and J.-B. Raina, Swimming towards each other: the role of chemo- taxis in bacterial interactions, *Trends Microbiology* **32**, 640 (2024).

[27] R. Fetecau and A. Guo, A mathematical model for flight guidance in honeybee swarms, *Bull. Math. Biol.* **74**, 2600 (2012).

[28] M. Beekman, R. L. Fathke, and T. D. Seeley, How does an informed minority of scouts guide a honeybee swarm as it flies to its new home?, *Anim. Behav.* **71**, 161 (2006).

[29] A. Sengupta, T. Kruppa, and H. Löwen, Chemotactic predator-prey dynamics, *Phys. Rev. E* **83**, 031914 (2011).

[30] N. J. Cira, A. Benusiglio, and M. Prakash, Vapour-mediated sensing and motility in two-component droplets, *Nature* **519**, 446 (2015).

[31] J. Bialké, T. Speck, and H. Löwen, Crystallization in a dense suspension of self-propelled particles, *Phys. Rev. Lett.* **108**, 168301 (2012).

[32] A. Wysocki, R. G. Winkler, and G. Gompper, Cooperative motion of active Brownian spheres in three-dimensional dense suspensions, *EPL (Europhys. Lett.)* **105**, 48004 (2014).

[33] M. E. Cates and J. Tailleur, Motility-induced phase separation, *Annu. Rev. Condens. Matter Phys.* **6**, 219 (2015).

[34] P. Digregorio, D. Levis, A. Suma, L. F. Cugliandolo, G. Gonnella, and I. Pagonabarraga, Full phase diagram of active Brownian disks: From melting to motility-induced phase separation, *Phys. Rev. Lett.* **121**, 098003 (2018).

[35] F. Peruani, A. Deutsch, and M. Bär, Nonequilibrium clustering of self-propelled rods, *Phys. Rev. E* **74**, 030904 (2006).

[36] M. Theers, E. Westphal, K. Qi, R. G. Winkler, and G. Gompper, Clustering of microswimmers: interplay of shape and hydrodynamics, *Soft Matter* **14**, 8590 (2018).

[37] J. Stenhammar, R. Wittkowski, D. Marenduzzo, and M. E. Cates, Activity-induced phase separation and self-assembly in mixtures of active and passive particles, *Phys. Rev. Lett.* **114**, 018301 (2015).

[38] A. Wysocki, R. G. Winkler, and G. Gompper, Propagating interfaces in mixtures of active and passive Brownian particles, *New J. Phys.* **18**, 123030 [1 (2016)].

[39] R. Wittkowski, J. Stenhammar, and M. E. Cates, Nonequilibrium dynamics of mixtures of active and passive colloidal particles, *New J. Phys.* **19**, 105003 (2017).

[40] T. Kolb and D. Klotza, Active binary mixtures of fast and slow hard spheres, *Soft Matter* **16**, 1967 (2020).

[41] D. P. Singh, U. Choudhury, P. Fischer, and A. G. Mark, Non-equilibrium assembly of light-activated colloidal mixtures, *Adv. Mater.* **29**, 1701328 (2017).

[42] M. Jhajhria, S. Sahoo, T. Biswas, and S. Thakur, Activity induced non-monotonic aggregation in a mixture of chemically active and passive particles, *Soft Materials* , 1 (2023).

[43] Z. Gao and I. D. Couzin, Swarming transitions of self-propelled particles with anisotropic social interactions, *Phys. Rev. Research* **7**, 023144 (2025).

[44] R. S. Negi, R. G. Winkler, and G. Gompper, Collective behavior of self-steering active particles with velocity alignment and visual perception, *Phys. Rev. Research* **6**, 013118 (2024).

[45] R. Saavedra, G. Gompper, and M. Ripoll, Swirling due to misaligned perception-dependent motility, *Phys. Rev. Lett.* **132**, 268301 (2024).

[46] I. D. Couzin, J. Krause, R. James, G. D. Ruxton, and N. R. Franks, Collective memory and spatial sorting in animal groups, *J. Theor. Biol.* **218**, 1 (2002).

[47] L. Barberis and F. Peruani, Large-scale patterns in a minimal cognitive flocking model: Incidental leaders, nematic patterns, and aggregates, *Phys. Rev. Lett.* **117**, 248001 (2016).

[48] R. S. Negi, R. G. Winkler, and G. Gompper, Emergent collective behavior of active Brownian particles with visual perception, *Soft Matter* **18**, 6167 (2022).

[49] Z. Liu and M. Dijkstra, Collective dynamics of intelligent active brownian particles with visual perception and velocity alignment in 3d: Spheres, rods, and worms, *Soft Matter* (2025).

[50] S. Chatterjee, M. Mangeat, C.-U. Woo, H. Rieger, and J. D. Noh, Flocking of two unfriendly species: The two-species vicsek model, *Phys. Rev. E* **107**, 024607 (2023).

[51] N. K. Agrawal and P. S. Mahapatra, Alignment-mediated segregation in an active-passive mixture, *Phys. Rev. E* **104**, 044610 (2021).

[52] J. Agudo-Canalejo and R. Golestanian, Active phase separation in mixtures of chemically interacting particles, *Phys. Rev. Lett.* **123**, 018101 (2019).

[53] S. Maity and A. Morin, Spontaneous demixing of binary colloidal flocks, *Phys. Rev. Lett.* **131**, 178304 (2023).

[54] S. Das, G. Gompper, and R. G. Winkler, Confined active Brownian particles: theoretical description of propulsion-induced accumulation, *New J. Phys.* **20**, 015001 (2018).

[55] S. Goh, R. G. Winkler, and G. Gompper, Noisy pursuit and pattern formation of self-steering active particles, *New J. Phys.* **24**, 093039 (2022).

[56] R. S. Negi, P. Iyer, and G. Gompper, Controlling inter-particle distances in crowds of motile, cognitive, active particles, *Sci. Rep.* **14**, 9443 (2024).

[57] P. Iyer, R. S. Negi, A. Schadschneider, and G. Gompper, Directed motion of cognitive active agents in a crowded three-way intersection, *Commun. Phys.* **7**, 379 (2024).

[58] O. Chepizhko, D. Saintillan, and F. Peruani, Revisiting the emergence of order in active matter, *Soft Matter* **17**, 3113 (2021).

[59] See Supplemental Material at [URL by publisher] for simulation movies..

[60] S. Mandal, B. Liebchen, and H. Löwen, Motility-induced temperature difference in coexisting phases, *Phys. Rev. Lett.* **123**, 228001 (2019).

[61] N. Grønbech-Jensen and O. Farago, A simple and effective verlet-type algorithm for simulating langevin dynamics, *Mol. Phys.* **111**, 983 (2013).

[62] N. Agmon, The grotthuss mechanism, *Chem. Phys. Lett.* **244**, 456 (1995).

[63] A picture of a reef shark in a school of fish was taken in 2012 in Australia by Scott Carr. See <https://iso.500px.com/parting-of-the-feast-behind-this-remarkable-photo-of-a-reef-shark-parting-a-school-of-fish/>.

[64] Y. Touahmi, N. Burlutskiy, K. Lee, and B. Lee, Congestion avoidance for multiple micro-robots using the behaviour of fish schools, *Int. J. Adv. Robotic Sy.* **9**, 67 (2012).

[65] A. C. Tsang, E. Demir, Y. Ding, and O. S. Pak, Roads to smart artificial microswimmers, *Adv. Intell. Syst.* **2**, 1900137 (2020).

[66] J. Chen, X. Lei, Y. Xiang, M. Duan, X. Peng, and H. P. Zhang, Emergent chirality and hyperuniformity in an active mixture with nonreciprocal interactions, *Phys. Rev. Lett.* **132**, 118301 (2024).

[67] M. Fruchart, R. Hanai, P. B. Littlewood, and V. Vitelli, Non-reciprocal phase transitions, *Nature* **592**, 363 (2021).

[68] T. Suchanek, K. Kroy, and S. A. M. Loos, Irreversible mesoscale fluctuations herald the emergence of dynamical phases, *Phys. Rev. Lett.* **131**, 258302 (2023).

[69] K. L. Kreienkamp and S. H. L. Klapp, Nonreciprocal alignment induces asymmetric clustering in active mixtures, *Phys. Rev. Lett.* **133**, 258303 (2024).

[70] Exemplary simulation datasets corresponding to all discussed parameter sets are available in the Zenodo repository: <https://doi.org/10.5281/zenodo.15208145>. Additional data can be provided by the authors upon reasonable request.